A Legendre spectral element method for the rotational Navier-Stokes equations

by

Anthony Harkin

Submitted to the Department of Mathematics
in partial fulfillment of the requirements for the degree of

Master of Science

at the

MASSACHUSETTS INSTITUTE OF TECHNOLOGY

May 1995

© Massachusetts Institute of Technology 1995. All rights reserved.

Author .....
Department of Mathematics
May 1995

Certified by .....
Fabian Waleffe
Assistant Professor of Mathematics
Thesis Supervisor

Certified by .....
Richard Stanley, Chairman
Applied Mathematics Committee

Accepted by .....
David Vogan, Chairman
Departmental Committee on Graduate Students

MASSACHUSETTS INSTITUTE
OF TECHNOLOGY
Science
OCT 20 1995

A Legendre spectral element method for the rotational Navier-Stokes equations

by

Anthony Harkin

Submitted to the Department of Mathematics
on May 18, 1995, in partial fulfillment of the
requirements for the degree of
Master of Science

Abstract

The objective of this work is to develop spectrally accurate numerical codes suitable for the computation of rotating flows in complex geometries. The primary focus of the computations is to assist in the design of a new centrifugal spectrometer. The numerical scheme employed is based on the spectral element method introduced by A. Patera [3] for the solution of incompressible flow problems of low to moderate Reynolds number. The method blends domain decomposition along with high order polynomial expansions over quadrilateral elements. The discretization is achieved through a weighted-residual technique using Gaussian quadrature.

The axisymmetric Stokes problem is presented as a natural prelude to the study of the fully nonlinear Navier-Stokes equations. In this fashion, it is determined that the viscous and pressure terms are to be treated implicitly, while the Coriolis term and nonlinear advection are treated explicitly. The classical Uzawa algorithm is used to invert the resulting discrete system. Lastly, numerical results pertinent to flow in the centrifugal spectrometer are presented.

Thesis Supervisor: Fabian Waleffe
Title: Assistant Professor of Mathematics

Acknowledgments

I would like to thank my advisor, Prof. Fabian Waleffe, for introducing me to the joys of scientific computation. I would also like to thank Dr. Sanjay Kumar for his useful suggestions in the early stages of this work.

Contents

1 Introduction **5**

2 Poisson's Equation (2-D) **7**

3 Axisymmetric Stokes Flow **12**

3.1 The Stokes Problem 12

3.2 Stokes Solver 14

3.3 The Rotating Stokes Problem 16

4 Axisymmetric Navier-Stokes **18**

4.1 Rotating Navier-Stokes Discretization 18

4.2 Numerical Results 20

Bibliography **23**

A Legendre-Lagrange Interpolants **24**

B Figures **26**

Chapter 1

Introduction

The impetus for this work is the computation of steady state solutions of flows in a centrifugal spectrometer. The centrifugal spectrometer [1] is a device to separate the constituents of a dilute suspension of non-interacting particles by mass or size. The sorting process involves diverting particles of differing sedimentation velocities through an internal nest of concentric, slotted cones [1]. Possible applications include the fractionation of viral factors or the industrial separation of latex beads. Therefore, any numerical simulation of the device requires a technique appropriate for rotational flow through complex geometries.

The spectral element method, as proposed by A. Patera [3], combines the accuracy of p-type spectral techniques with the geometric flexibility of h-type finite element methods. The spectral element discretization of a complex geometry involves breaking the computational domain into K quadrilateral elements over which vector and scalar unknowns are approximated by N^{th}-order tensor-product polynomial expansions. The governing partial differential equations for the fluid flow are then cast into *weak form* and Gaussian quadrature is performed to arrive at a symmetric saddle problem. This saddle problem can then be decoupled into two symmetric positive-definite forms which are inverted through standard conjugate gradient iterations.

For infinitely smooth solutions and data the spectral element method converges

[1] H.P. Greenspan, US patent #4,842,738

exponentially to the exact solution as the order of the polynomial approximation, N, increases (p-type approach) and the number of elements, K, remains fixed [2]. Therefore, the method is well suited to incompressible flow problems of low to moderate Reynolds number. Exponential convergence to an exact solution of the forced Burgers' equation is demonstrated in figure B-1. Alternatively, algebraic convergence may be achieved as the order of the polynomial approximation is held fixed while the number of elements increases and this then becomes an h-type finite element method. Although the work per degree-of-freedom increases as the order of a p-type method increases, many fewer degrees-of-freedom are required to achieve a fixed level of error than by an h-type method. Thus, the exponential convergence of the spectral element method is not accompanied by a decrease in efficiency relative to h-type schemes.

Chapter 2

Poisson's Equation (2-D)

The fundamental ideas of the spectral element method can be illustrated more simply with Poisson's equation on a two-dimensional domain, Ω, with homogeneous Dirichlet conditions on the boundary, $\partial\Omega$

$$-\Delta u = f \quad in \quad \Omega, \tag{2.1}$$

$$u = 0 \quad on \quad \partial\Omega. \tag{2.2}$$

Here $\Delta = \nabla^2$ is the cartesian Laplace operator. The discretization is based on the Rayleigh-Ritz idea of casting the equation into *Galerkin weak form.* This procedure amounts to multiplying (2.1) by an arbitrary test function, (v), and integration by parts over the domain, Ω, which yields

$$\int_\Omega \nabla u \cdot \nabla v \, dA = \int_\Omega f v \, dA + \oint_{\partial\Omega} v \frac{\partial u}{\partial \hat{n}} \, ds, \quad \forall v. \tag{2.3}$$

The weak form (2.3) is an alternate formulation of the *strong form* (2.1). The term *weak* refers to the fact that (2.3) allows a larger class of solutions such that ∇^2 need not exist everywhere.

The last term in (2.3) is determined by specifying either Neumann or Dirichlet conditions on the boundary of Ω. Specifying Neumann boundary conditions effectively contributes to the forcing on the right hand side. On the other hand, if the value of the

function (u) is imposed on the boundary then, in accordance with the Rayleigh-Ritz discretization procedure, there is no need to test the variational response of points on the boundary with respect to the test function and (v) will be chosen zero there. Hence, for Dirichlet conditions the boundary term in (2.3) does not contribute to the forcing on the right hand side and the *weak form* of equation (2.1) becomes

$$\int_\Omega \nabla u \cdot \nabla v \, dA = \int_\Omega f v \, dA, \tag{2.4}$$

for all functions (v) with $v = 0$ on $\partial\Omega$.

The next step in the spectral element discretization is to break up the domain, Ω, into K disjoint, conforming quadrilateral elements, (e.g. figure B-7)

$$\Omega = \bigcup_{k=1}^{K} \bar{\Omega}_k. \tag{2.5}$$

The discrete system corresponding to (2.4) is obtained by mapping each element, $\bar{\Omega}_k$, to a reference domain over which the integration is performed using Gauss-Lobatto Legendre quadrature. The contributions from each element are then summed together. If we define

$$a^k(u,v) = \int_{\bar{\Omega}_k} \nabla u \cdot \nabla v \, dxdy, \tag{2.6}$$

and

$$(f,v)^k = \int_{\bar{\Omega}_k} f v \, dxdy, \tag{2.7}$$

then (2.4) becomes

$$\sum_{k=1}^{K} a^k(u,v) = \sum_{k=1}^{K} (f,v)^k. \tag{2.8}$$

The elemental integrals in (2.6) can be rewritten with respect to the reference element (bilinear) mapping, $(x,y) \in \bar{\Omega}_k \mapsto (\eta,\xi) \in [-1,1] \times [-1,1]$, as

$$a^k(u,v) = \int_{-1}^{1}\int_{-1}^{1} \tilde{\nabla} u^k(\eta,\xi) \cdot \tilde{\nabla} v^k(\eta,\xi) \, |J^k(\eta,\xi)| \, d\eta d\xi, \tag{2.9}$$

where

$$\tilde{\nabla} = \left(\frac{\partial \eta}{\partial x}\frac{\partial}{\partial \eta} + \frac{\partial \xi}{\partial x}\frac{\partial}{\partial \xi}\right)\hat{\mathbf{i}} + \left(\frac{\partial \eta}{\partial y}\frac{\partial}{\partial \eta} + \frac{\partial \xi}{\partial y}\frac{\partial}{\partial \xi}\right)\hat{\mathbf{j}}, \tag{2.10}$$

and

$$J = \left(\frac{\partial x}{\partial \eta}\frac{\partial y}{\partial \xi} - \frac{\partial x}{\partial \xi}\frac{\partial y}{\partial \eta}\right). \tag{2.11}$$

Similarly, (2.7) can be rewritten in the mapped variables

$$(f, v)^k = \int_{-1}^{1}\int_{-1}^{1} f^k(\eta, \xi) v^k(\eta, \xi) \left|J^k(\eta, \xi)\right| d\eta d\xi. \tag{2.12}$$

As stated in the introduction, a high order tensor-product polynomial expansion is used to approximate the solution over each element

$$u^k(\eta, \xi) = \sum_{i=0}^{N}\sum_{j=0}^{N} u_{ij}^k T_i(\eta) T_j(\xi) \tag{2.13}$$

where u_{ij}^k is the value of (u) at point (η_i, ξ_j) inside the (mapped) element, $\bar{\Omega}_k$, and T_i is an N^{th}-order Lagrangian interpolant through the Gauss-Lobatto Legendre points (see appendix A and figure B-2). The choice of the Gauss-Lobatto Legendre points serves two purposes. First, because we began the discretization with the *weak form* of the equation (2.3) we only need to impose continuity of (u) across elemental boundaries. This is accomplished in a natural way by selecting Gauss-Lobatto points and Lagrange interpolants. Second, the orthogonal properties of the Legendre polynomials preserve the symmetry of the original self-adjoint equation (2.1). Typically in Galerkin variational solution techniques the test functions, (v), are chosen from the basis used to approximate the solution (2.13) such that they are nonzero at only one global collocation point. This is needed in order to preserve the symmetry in the discrete system. For this reason the test functions are chosen to be

$$v^k(\eta, \xi) = T_p(\eta) T_q(\xi), \qquad p, q \in (0, \ldots, N). \tag{2.14}$$

If the expansion (2.13) and test functions (2.14) are inserted into the elemental integral (2.9) and Gauss-Lobatto quadrature is performed then $\forall p, q \in (0, \ldots, N)$ we

have

$$
\begin{aligned}
a^k_{pq}(u,v) &= \sum_{m=0}^{N}\left[T'_p(\eta_m)\left(\eta_x^2+\eta_y^2\right)_{m,q}|J(\eta_m,\xi_q)|w_m w_q\left[\sum_{i=0}^{N}u^k_{iq}T'_i(\eta_m)\right]\right]+ \\
&\quad \sum_{n=0}^{N}\left[T'_q(\xi_n)\left(\xi_x^2+\xi_y^2\right)_{p,n}|J(\eta_p,\xi_n)|w_p w_n\left[\sum_{j=0}^{N}u^k_{pj}T'_j(\xi_n)\right]\right]+ \\
&\quad \sum_{j=0}^{N}\left[T'_q(\xi_j)\left(\eta_x\xi_x+\eta_y\xi_y\right)_{p,j}|J(\eta_p,\xi_j)|w_p w_j\left[\sum_{i=0}^{N}u^k_{ij}T'_i(\eta_p)\right]\right]+ \\
&\quad \sum_{i=0}^{N}\left[T'_p(\eta_i)\left(\eta_x\xi_x+\eta_y\xi_y\right)_{i,q}|J(\eta_i,\xi_q)|w_i w_q\left[\sum_{j=0}^{N}u^k_{ij}T'_j(\xi_q)\right]\right] \qquad (2.15) \\
&= \sum_{i=0}^{N}\sum_{j=0}^{N}\mathbf{A}^k_{pqij}u^k_{ij}, \qquad (2.16)
\end{aligned}
$$

where the w_i are the weights associated with the quadrature rule. To complete the discretization, (2.13) and (2.14) are inserted into (2.12) and quadrature is again performed $\forall p,q \in (0,\ldots,N)$

$$
\begin{aligned}
(f,v)^k_{pq} &= \sum_{i=0}^{N}\sum_{j=0}^{N}f^k(\eta_i,\xi_j)T_p(\eta_i)T_q(\xi_j)|J(\eta_i,\xi_j)|w_i w_j \qquad (2.17) \\
&= \sum_{i=0}^{N}\sum_{j=0}^{N}\mathbf{B}^k_{pqij}f^k_{ij}. \qquad (2.18)
\end{aligned}
$$

The system

$$
\sum_{k=1}^{K}\sum_{i=0}^{N}\sum_{j=0}^{N}\mathbf{A}^k_{pqij}u^k_{ij} = \sum_{k=1}^{K}\sum_{i=0}^{N}\sum_{j=0}^{N}\mathbf{B}^k_{pqij}f^k_{ij} \qquad (2.19)
$$

for all p,q, is assembled by the elimination of nodes corresponding to essential boundary conditions and summing the contributions of rows and columns corresponding to global nodes that lie on elemental interfaces. This assembly procedure is often referred to as *direct stiffness summation* in the context of finite elements.

Thanks to the orthogonal properties of the Legendre polynomials the matrix $\mathbf{A}$ is symmetric positive-definite which allows the use of the conjugate gradient algorithm to solve the system. In doing so the algorithm requires successive evaluations of the matrix-vector product $\mathbf{Au}$ which, if done naively, can cost $O(KN^4)$ operations. A clever evaluation of (2.15) can be done in $O(KN^3)$ operations and this *tensor-product*

factorization is essential for the efficiency of any high order method [4]. The key to evaluating (2.15) is to first compute the innermost bracketed terms for all p, q and then to use them to evaluate the outermost bracketed terms. In three dimensions the gain in efficiency is even greater, a naive evaluation of the matrix-vector product would consume $O(KN^6)$ operations as opposed to $O(KN^4)$ work for the clever approach.

Numerical evidence suggests that the method converges exponentially to the exact solution even in relatively deformed elements [5]. In figures B-3 and B-4, eigenmodes of $\Delta \equiv \mathbf{B}^{-1}\mathbf{A}$ are computed on two different deformed geometries.

Chapter 3

Axisymmetric Stokes Flow

3.1 The Stokes Problem

The accurate and efficient computation of Stokes flow

$$-\nu\nabla^2\mathbf{u} + \nabla p = \mathbf{f} \tag{3.1}$$

$$-\nabla\cdot\mathbf{u} = 0 \tag{3.2}$$

serves as a precursor to applying a numerical method to the Navier-Stokes equations. This is especially true for the inherently *variational* spectral element method since the Stokes problem in fact can be formulated as a constrained minimization problem. Furthermore, the solution algorithm that will be employed to invert the discrete system first arose in the context of constrained optimization. The weak form of (3.1)-(3.2) with Dirichlet boundary conditions is

$$\nu\int_\Omega \nabla\mathbf{u} : \nabla\boldsymbol{\Psi}\, dV - \int_\Omega p\nabla\cdot\boldsymbol{\Psi}\, dV = \int_\Omega \mathbf{f}\cdot\boldsymbol{\Psi}\, dV \tag{3.3}$$

$$-\int_\Omega \Phi(\nabla\cdot\mathbf{u})\, dV = 0 \tag{3.4}$$

where

$$\nabla = \hat{\mathbf{e}}_r\frac{\partial}{\partial r} + \hat{\mathbf{e}}_\theta\frac{1}{r}\frac{\partial}{\partial\theta} + \hat{\mathbf{e}}_z\frac{\partial}{\partial z}. \tag{3.5}$$

Note that $\mathbf{\Psi}$ is a vector test function while Φ is a scalar test function. The axisymmetric domain, Ω, is broken up as in the Poisson case into quadrilateral subdomains, $\bar{\Omega}_k$.

Continuing with the discretization procedure we introduce an N^{th}-order tensor-product polynomial expansion for the axisymmetric velocity

$$\mathbf{u}_m^k = \sum_{i=0}^{N}\sum_{j=0}^{N} \mathbf{u}_{mij}^k T_i(\eta) T_j(\xi) \tag{3.6}$$

where $m = 1, 2, 3$ represent the radial, azimuthal and vertical components of velocity respectively. The basis functions for the velocity are based upon the $N+1$ Gauss-Lobatto points. The null space of the discrete gradient operator can contain non constant vectors, the so-called spurious modes. To avoid this problem a tensor-product polynomial expansion of order $N-2$ is sought for the pressure [6]

$$p^k = \sum_{i=1}^{N-1}\sum_{j=1}^{N-1} p_{ij}^k \tilde{T}_i(\eta)\tilde{T}_j(\xi). \tag{3.7}$$

In general, for the spectral element method the space of p^k should be two orders less than that for $\mathbf{u}$ to avoid spurious modes. The basis used to expand the pressure can be based upon the roots of the Legendre polynomial of order $N-1$ (Gauss points). This is similar to a staggered grid approach because the pressure nodes do not coincide with the velocity nodes [7]. Alternatively, the pressure can be approximated by using the $N-1$ interior Gauss-Lobatto points. Then the pressure nodes coincide with the interior velocity nodes and as a result a gain in efficiency is obtained when computing the action of the discrete gradient operator on the pressure.

The test vectors for the velocity are, $\forall r, s \in (0, \ldots, N)$

$$\mathbf{\Psi}_1 = \begin{bmatrix} T_r T_s \\ 0 \\ 0 \end{bmatrix}, \quad \mathbf{\Psi}_2 = \begin{bmatrix} 0 \\ T_r T_s \\ 0 \end{bmatrix}, \quad \mathbf{\Psi}_3 = \begin{bmatrix} 0 \\ 0 \\ T_r T_s \end{bmatrix} \tag{3.8}$$

and quadrature corresponding to the velocity and the forcing is done using the Gauss-

Lobatto points. The test functions associated with the divergence operator are $\forall r, s \in (1, \ldots, N-1)$

$$\Phi = \tilde{T}_r \tilde{T}_s \tag{3.9}$$

Numerical quadrature corresponding to the pressure and the divergence operator can be performed using the Gauss points [8] or by using Gauss-Lobatto points.

The discretization based upon the weak form (3.3)-(3.4) gives rise to the symmetric linear system

$$\begin{pmatrix} \mathbf{A}_1 & 0 & 0 & -\mathbf{D}_1 \\ 0 & \mathbf{A}_1 & 0 & 0 \\ 0 & 0 & \mathbf{A}_3 & -\mathbf{D}_3 \\ -\mathbf{D}_1^T & 0 & -\mathbf{D}_3^T & 0 \end{pmatrix} \begin{pmatrix} \mathbf{u} \\ \mathbf{v} \\ \mathbf{w} \\ \mathbf{p} \end{pmatrix} = \begin{pmatrix} \mathbf{f}_1 \\ \mathbf{f}_2 \\ \mathbf{f}_3 \\ 0 \end{pmatrix} \tag{3.10}$$

where $\mathbf{A}$ is the variational equivalent of the Laplace operator and $\mathbf{D} = (\mathbf{D}_1^T, \mathbf{0}, \mathbf{D}_3^T)^T$ is the discrete gradient operator. If the axis of symmetry belongs to the domain, Ω, then the symmetry conditions $u = 0, v = 0$, and $\frac{\partial w}{\partial r} = 0$ at $r = 0$ are imposed, and rows that correspond to nodes on $r = 0$ are appended to $\mathbf{A}_3, \mathbf{D}_3$ and $\mathbf{f}_3$. Even though $\mathbf{w}$ needs to be computed at $r = 0$, the boundary term in the weak form still vanishes because the differential unit of volume in cylindrical coordinates, $rdrd\theta dz$, contains a factor of r.

Figure B-5 demonstrates the *local refinement* feature of the spectral element technique applied to Stokes flow. This allows additional grid points to be placed near regions where the solution is not well behaved (such as near re-entrant corners) or where greater accuracy is desired.

3.2 Stokes Solver

The classical Uzawa algorithm is used to solve the system (3.10) which involves block Gaussian elimination to first solve for the pressure

$$(\mathbf{D}_1^T \mathbf{A}_1^{-1} \mathbf{D}_1 + \mathbf{D}_3^T \mathbf{A}_3^{-1} \mathbf{D}_3)\mathbf{p} = -(\mathbf{D}_1^T \mathbf{A}_1^{-1} \mathbf{f}_1 + \mathbf{D}_3^T \mathbf{A}_3^{-1} \mathbf{f}_3) \tag{3.11}$$

and then back substitution to obtain $\mathbf{u}, \mathbf{v}$ and $\mathbf{w}$. The system (3.11) has the form $\mathbf{Sp} = \mathbf{f}'$ where the matrix $\mathbf{S} = (\mathbf{D}_1^T \mathbf{A}_1^{-1} \mathbf{D}_1 + \mathbf{D}_3^T \mathbf{A}_3^{-1} \mathbf{D}_3)$ is symmetric positive-definite. Therefore, standard preconditioned conjugate gradient iterations can be used to solve for the pressure as follows:

$$\mathbf{p}_0; \quad \mathbf{r}_0 = \mathbf{f}' - \mathbf{S}\mathbf{p}_0; \quad \mathbf{q}_0 = \mathbf{P}^{-1}\mathbf{r}_0; \quad \mathbf{d}_0 = \mathbf{q}_0;$$

while $\mathbf{r}_m^T \mathbf{r}_m > \epsilon \mathbf{f}'^T \mathbf{f}'$

$$\begin{aligned}
\alpha &= \frac{\mathbf{q}_m^T \mathbf{r}_m}{\mathbf{d}_m^T \mathbf{S} \mathbf{d}_m} \\
\mathbf{p}_{m+1} &= \mathbf{p}_m + \alpha \mathbf{d}_m \\
\mathbf{r}_{m+1} &= \mathbf{r}_m - \alpha \mathbf{S} \mathbf{d}_m \\
\mathbf{q}_{m+1} &= \mathbf{P}^{-1} \mathbf{r}_{m+1} \\
\beta &= \frac{\mathbf{q}_{m+1}^T \mathbf{r}_{m+1}}{\mathbf{q}_m^T \mathbf{r}_m} \\
\mathbf{d}_{m+1} &= \mathbf{q}_{m+1} + \beta \mathbf{d}_m
\end{aligned} \tag{3.12}$$

end

where m is the iteration number, ϵ is the tolerance factor, $\mathbf{r}_m$ is the residual, $\mathbf{d}_m$ is the search direction, $\mathbf{q}_m$ is the preconditioning vector and $\mathbf{P}$ is the preconditioner. Most of the computational cost of the algorithm is consumed in forming the matrix-vector product $\mathbf{S}\mathbf{d}_m$ which requires the inversion of $\mathbf{A}$ for each conjugate gradient iteration. The inversion of $\mathbf{A}$ can in turn be accomplished with conjugate gradient iterations. Hence, the Uzawa scheme is a *nested* algorithm. To see this let

$$\mathbf{y}_i = \mathbf{D}_i \mathbf{d}_m \tag{3.13}$$

where $i = 1, 2$. Now, if $\mathbf{x}_i$, $i = 1, 2$ satisfies

$$\mathbf{A}_i \mathbf{x}_i = \mathbf{y}_i \tag{3.14}$$

then the matrix-vector product can be written as

$$\mathbf{S}\mathbf{d}_m = \sum_{i=1}^{2} \mathbf{D}_i^T \mathbf{x}_i. \tag{3.15}$$

The computational complexity to invert (3.14) is $O(KN^{d+1})$ in $\Re^d$ if the tensor-product factorization scheme is used to compute $\mathbf{A}_i \mathbf{x}_i$.

The efficiency of the Uzawa decoupling scheme for Stokes flow relies on the fact that the system (3.11) is extremely well-conditioned. Since $\mathbf{A}^{-1}$ is essentially the inverse of a Laplacian and $\mathbf{D}$ is the variational gradient operator then $\nu\tilde{\mathbf{B}}^{-1}(\mathbf{D}_1^T\mathbf{A}_1^{-1}\mathbf{D}_1 + \mathbf{D}_3^T\mathbf{A}_3^{-1}\mathbf{D}_3)$ is identity-like with regards to its spectrum where $\tilde{\mathbf{B}}$ is the diagonal mass matrix associated with the pressure nodes. Thus, for (3.12) the preconditioner is $\mathbf{P} = (1/\nu)\tilde{\mathbf{B}}$.

3.3 The Rotating Stokes Problem

The Stokes problem in a rotating frame

$$-\nu\nabla^2\mathbf{u} + 2\boldsymbol{\Omega} \times \mathbf{u} + \nabla p = \mathbf{f} \tag{3.16}$$

$$-\nabla \cdot \mathbf{u} = 0 \tag{3.17}$$

leads to a discretization of the form

$$\begin{pmatrix} \mathbf{A}_1 & -2\Omega\mathbf{B}_1 & 0 & -\mathbf{D}_1 \\ -2\Omega\mathbf{B}_1 & -\mathbf{A}_1 & 0 & 0 \\ 0 & 0 & \mathbf{A}_3 & -\mathbf{D}_3 \\ -\mathbf{D}_1^T & 0 & -\mathbf{D}_3^T & 0 \end{pmatrix} \begin{pmatrix} \mathbf{u} \\ \mathbf{v} \\ \mathbf{w} \\ \mathbf{p} \end{pmatrix} = \begin{pmatrix} \mathbf{f}_1 \\ -\mathbf{f}_2 \\ \mathbf{f}_3 \\ 0 \end{pmatrix}. \tag{3.18}$$

After elimination of $\mathbf{v}$ from the second row, $\mathbf{v} = \mathbf{A}_1^{-1}(\mathbf{f}_2 - 2\Omega\mathbf{B}_1\mathbf{u})$, the nested Uzawa iterations can again be used to solve for the pressure

$$[\mathbf{D}_1^T(\mathbf{A}_1 + 4\Omega^2\mathbf{B}_1\mathbf{A}_1^{-1}\mathbf{B}_1)^{-1}\mathbf{D}_1 + \mathbf{D}_3^T\mathbf{A}_3^{-1}\mathbf{D}_3]\mathbf{p} = \mathbf{f}' \tag{3.19}$$

where $\mathbf{f}' = -[\mathbf{D}_1^T(\mathbf{A}_1 + 4\Omega^2\mathbf{B}_1\mathbf{A}_1^{-1}\mathbf{B}_1)^{-1}(\mathbf{f}_1 + 2\Omega\mathbf{B}_1\mathbf{A}_1^{-1}\mathbf{f}_2) + \mathbf{D}_3^T\mathbf{A}_3^{-1}\mathbf{f}_3]$. Most of the effort solving (3.19) is spent on the inversion of $\mathbf{A}_1 + 4\Omega^2\mathbf{B}_1\mathbf{A}_1^{-1}\mathbf{B}_1$. To accomplish this we can rewrite

$$\left(\mathbf{A}_1 + 4\Omega^2\mathbf{B}_1\mathbf{A}_1^{-1}\mathbf{B}_1\right)\mathbf{x} = \mathbf{y} \tag{3.20}$$

as

$$\left(\mathbf{A}_1\mathbf{B}_1^{-1}\mathbf{A}_1 + 4\Omega^2\mathbf{B}_1\right)\mathbf{x} = \mathbf{A}_1\mathbf{B}_1^{-1}\mathbf{y} \tag{3.21}$$

and solve using preconditioned conjugate gradient iterations with

$$\mathbf{P} = \mathbf{B}_1^{-1}[diag(\mathbf{A}_1)]^2 + 4\Omega^2\mathbf{B}_1. \tag{3.22}$$

The addition of the Coriolis term to the discretization of the Stokes problem destroys the almost perfect conditioning of the system. This is an area of considerable interest and a great deal of attention has been paid to resolve the issue. To date, an effective preconditioner for (3.19) has not been found. As a consequence the Coriolis term must be treated explicitly when solving unsteady Stokes or Navier-Stokes problems. In fact, although the implicit treatment of the Coriolis term in the Navier-Stokes equations removes the stability restriction $\Delta t < 1/\Omega$, it is often necessary to keep $\Delta t \approx 1/\Omega$ if inertial waves that may be present are to be accurately resolved.

Chapter 4

Axisymmetric Navier-Stokes

4.1 Rotating Navier-Stokes Discretization

The spectral element method can be readily extended to the (non-dimensional) Navier-Stokes equations in a rotating frame

$$\frac{\partial \mathbf{u}}{\partial t} + 2\mathbf{k} \times \mathbf{u} + \mathcal{R}_0 \mathbf{u} \cdot \nabla \mathbf{u} = -\nabla P + E \nabla^2 \mathbf{u} \tag{4.1}$$

$$\nabla \cdot \mathbf{u} = 0 \tag{4.2}$$

where $\mathbf{k}$ is the unit vector along the axis of rotation, $\mathcal{R}_0 = V/(\Omega H)$ is the Rossby number and $E = \nu/(\Omega H^2)$ is the Ekman number. The characteristic length scale, H, is given by the height of the axial channels in the centrifuge and the characteristic velocity, V, is determined by the volumetric throughput of flow in a single channel. A spectral element discretization is used for the spatial operators and, since we are interested in steady flows, backward Euler is used for the time integration, $\frac{\partial \mathbf{u}}{\partial t} = \sigma(\mathbf{u}^{N+1} - \mathbf{u}^N)$ where $\sigma = 1/\Delta t$. The Coriolis term and the nonlinear advection are treated explicitly as to maintain the symmetry and conditioning of the resulting

system

$$\begin{pmatrix} \mathbf{A}_1 + \sigma\mathbf{B}_1 & 0 & 0 & -\mathbf{D}_1 \\ 0 & \mathbf{A}_1 + \sigma\mathbf{B}_1 & 0 & 0 \\ 0 & 0 & \mathbf{A}_3 + \sigma\mathbf{B}_3 & -\mathbf{D}_3 \\ -\mathbf{D}_1^T & 0 & -\mathbf{D}_3^T & 0 \end{pmatrix} \begin{pmatrix} \mathbf{u} \\ \mathbf{v} \\ \mathbf{w} \\ \mathbf{p} \end{pmatrix}^{N+1} = \begin{pmatrix} \mathbf{f}_1 \\ \mathbf{f}_2 \\ \mathbf{f}_3 \\ \mathbf{f}_4 \end{pmatrix} \tag{4.3}$$

where

$$\begin{pmatrix} \mathbf{f}_1 \\ \mathbf{f}_2 \\ \mathbf{f}_3 \\ \mathbf{f}_4 \end{pmatrix} = \begin{pmatrix} \sigma\mathbf{u} + 2\mathbf{B}_1\mathbf{v} - \mathbf{\Lambda}_1 \\ \sigma\mathbf{v} - 2\mathbf{B}_1\mathbf{u} - \mathbf{\Lambda}_2 \\ \sigma\mathbf{w} - \mathbf{\Lambda}_3 \\ 0 \end{pmatrix}^N \tag{4.4}$$

and $\mathbf{\Lambda}$ is the advective term which can be easily computed using the interpolation formula for the velocity (3.6). Block Gaussian elimination leads to a system for the pressure

$$[\mathbf{D}_1^T(\mathbf{A}_1 + \sigma\mathbf{B}_1)^{-1}\mathbf{D}_1 + \mathbf{D}_3^T(\mathbf{A}_3 + \sigma\mathbf{B}_3)^{-1}\mathbf{D}_3]\mathbf{p}^{N+1} = \mathbf{f}_p^N \tag{4.5}$$

that can be inverted in a nested fashion at each time step. Considering the limits of small and large Δt, Ronquist [8] proposed an extremely effective preconditioner for (4.5)

$$\mathbf{P}^{-1} = \nu\tilde{\mathbf{B}}^{-1} + \frac{1}{\Delta t}\left(\mathbf{D}_1^T\mathbf{B}_1^{-1}\mathbf{D}_1 + \mathbf{D}_3^T\mathbf{B}_3^{-1}\mathbf{D}_3\right)^{-1}. \tag{4.6}$$

The scheme, as proposed, is only first order accurate in time since steady solutions are desired, however the algorithm can be easily enhanced to be second order accurate in time with, for example, Runge-Kutta

Step 1

$$2\sigma\left(\tilde{\mathbf{u}} - \mathbf{u}^n\right) + 2\mathbf{k} \times \mathbf{u}^n + \mathcal{R}_0\mathbf{u}^n\nabla\mathbf{u}^n = -\nabla\tilde{p} + E\nabla^2\tilde{\mathbf{u}}$$

$$\nabla \cdot \tilde{\mathbf{u}} = 0$$

Step 2

$$\sigma\left(\mathbf{u}^{n+1}-\mathbf{u}^{n}\right)+2\mathbf{k}\times\tilde{\mathbf{u}}+\mathcal{R}_0\tilde{\mathbf{u}}\nabla\tilde{\mathbf{u}}=-\nabla p^{n+\frac{1}{2}}+\frac{E}{2}\left(\nabla^2\mathbf{u}^{n+1}+\nabla^2\mathbf{u}^{n}\right)$$

$$\nabla\cdot\mathbf{u}^{n+1}=0$$

4.2 Numerical Results

The following figures show test cases and results pertinent to flow in the centrifugal spectrometer. In all cases, the computation is axisymmetric and fully nonlinear. The inflow profile for all figures involving flow through axial channels is obtained from the exact solution of steady laminar flow in a cylindrical annulus

$$w(r)=\frac{c_1}{4}\left[b^2-r^2+\frac{b^2-a^2}{\ln(a/b)}\ln\frac{b}{r}\right] \tag{4.7}$$

where a and b are the radii of the inner and outer concentric cylinders respectively. The constant, c_1, is evaluated using the expression for the flux

$$Q=\frac{c_1\pi}{8}\left[b^4-a^4-\frac{\left(b^2-a^2\right)^2}{\ln(b/a)}\right]. \tag{4.8}$$

The first test case (figure B-6) is the differential spin-up of fluid in a cylinder. The bottom and walls of the container rotate at a rate Ω while the top rotates slightly faster at a rate 1.3Ω and the Ekman number is 0.1. The computation is done with one element over which the solution is approximated by a polynomial expansion of order 10.

The next test case demonstrates the natural decomposition of a complex geometry into multiple elements. The problem of figure B-7 is spin-up from rest in an "hourglass" shaped container. The weak secondary circulation for an Ekman number of 1 is shown at time $t=0.2$ in the $r-z$ plane.

Exponential convergence of the spectral element method applied to the rotational Navier-Stokes equations is confirmed numerically in figure B-8. The time iteration given by (4.3)-(4.4) is allowed to run long enough such that the temporal error in the steady state solution is negligible.

Figure B-9 originally appeared in [1] and is reproduced using the spectral element code. The numerical scheme employed in [1] used the assumption that the Navier-Stokes equations in curvilinear coordinates are well approximated by their cartesian counterparts for a sufficiently large radius. Furthermore, the code was tailor-made for the specific geometry at hand. A spectral element implementation has neither of these two limitations. In both figures B-9(a) and (b), the flux is introduced at the bottom of the inner channel and withdrawn at the top of the outer channel. The specifications for the geometry are as follows. The width of a single channel, d, is 0.284, the total height of a channel, $2H$, is 2 and the slot width, $2L$, is 0.13. The computation was done for two different values of the Rossby number to illustrate the effects of nonlinearity. Contours of constant azimuthal velocity are drawn.

Competing ideas for the design of the centrifuge are explored in the following figures. In figure B-10 fluid is introduced into the tops of the two channels in equal amounts and withdrawn at equal rates from the bottom of the channels. This is the wash channel mode of operation because only particles, and not flux, are being diverted through the slot. On the other hand, in figure B-11 half of the flux that is introduced at the top of the inner channel is diverted to an outer channel. The device originally proposed in [1] was cylindrical whereas the current prototype is conical. Therefore, the channels in both figures are slanted 35 degrees to the vertical. The specifications for both figures are $d = 0.175$, $H = 1.0$ and the radius to the bottom of the inner channel is 1.5. The slot thickness for figure B-10 is 0.065 and 0.1 for figure B-11. Contours of constant azimuthal velocity and streamlines are plotted.

Current simulations concern a forty channel condensing centrifuge at the bottom of the main device (figure B-12). Fluid and particles enter the outer channel at the top. A small amount of fluid and, hopefully, all of the particles exit at the bottom while the rest of the fluid turns and goes up the forty channels into the innermost channel

where it exits at the top. Computational restrictions only allow the simulation of a ten channel device shown in figure B-13 for which the flow field has been obtained. Pressure and flux statistics are plotted for the set-up of figure B-13 in figures B-14 and B-15 respectively.

Bibliography

[1] A.A. Dahlkild, G. Amberg and H.P. Greenspan, "Flow in the centrifugal spectrometer," *J. Fluid Mech.* **238**, 221-250, 1992.

[2] Y. Maday and A.T. Patera, "Spectral element methods for the incompressible Navier-Stokes equations," In A.K. Noor, Editor, *State-of-the-art surveys in computational mechanics*, ASME, New York, 1988.

[3] A.T. Patera, "A spectral element method for Fluid Dynamics; Laminar flow in a channel expansion," *J. Comput. Phys.* **54**, 1984.

[4] S.A. Orszag, "Spectral methods for problems in complex geometries," *J. Comput. Phys.* **37**, 1980.

[5] E.M. Ronquist and A.T. Patera, "A Legendre spectral element method for the Stefan problem," *Int. J. Num. Methods Eng.* **24**, 1987.

[6] Y. Maday, A.T. Patera and E.M. Ronquist, "The $P_N \times P_{N-2}$ method for the approximation of the Stokes problem," *preprint*, 1992.

[7] C. Bernardi and Y. Maday, "A collocation method over staggered grids for the Stokes problem," *Int. J. Numer. Meth. in Fluids* **8**, 537-557, 1988.

[8] E.M. Ronquist, "Optimal spectral element methods for the unsteady three-dimensional incompressible Navier-Stokes equations," Ph.D. Thesis, Massachusetts Institute of Technology, 1988.

Appendix A

Legendre-Lagrange Interpolants

The Legendre polynomials, $L_k(x)$, satisfy

$$\frac{d}{dx}\left[(1-x^2)\frac{dL_k(x)}{dx}\right] + k(k+1)L_k(x) = 0 \tag{A.1}$$

and the three-term recurrence relation

$$L_{k+1}(x) = \frac{2k+1}{k+1}xL_k(x) - \frac{k}{k+1}L_{k-1}(x) \tag{A.2}$$

where $L_0(x) = 1$ and $L_1(x) = x$. The Legendre-Lagrange interpolant is given by, $\forall j = 0, \ldots, N$

$$T_j(x) = \frac{(1-x^2)L'_N(x)}{N(N+1)L_N(x_j)(x-x_j)} \tag{A.3}$$

such that $T_j(x_i) = \delta_{ij}$ (Kronecker delta) defines a set of collocation points. Any N^{th}-order polynomial on $[-1,1]$ can be written as

$$u(x) = \sum_{j=0}^{N} u_j T_j(x) \tag{A.4}$$

where u_j is the value of the polynomial at collocation point x_j. The derivative of $u(x)$ at $x = x_i$ can be expressed as

$$u'(x_i) = \sum_{j=0}^{N} u_j T'_j(x_i) \tag{A.5}$$

where

$$T_j'(x_i) = \begin{cases} \frac{L_n(x_i)}{L_N(x_j)(x_i - x_j)} & , \quad i \neq j \\ 0 & , \quad i = j, i \neq 0, N \\ \frac{-N(N+1)}{4} & , \quad i = j = 0 \\ \frac{N(N+1)}{4} & , \quad i = j = N \end{cases} \tag{A.6}$$

Let $x_0 = -1, x_N = 1$ and $x_j (j = 1, \ldots, N-1)$ be chosen as the zeroes of $L_N'(x)$. If we define quadrature weights by

$$w_j = \frac{2}{N(N+1)[L_N(x_j)]^2}, \quad j = 0, \ldots, N \tag{A.7}$$

then

$$\int_{-1}^{1} p(x) w(x)\, dx = \sum_{j=0}^{N} p(x_j) w_j \tag{A.8}$$

with $w(x) = 1$ is exact for all polynomials of degree $2N - 1$ (Gauss-Lobatto).

Appendix B

Figures

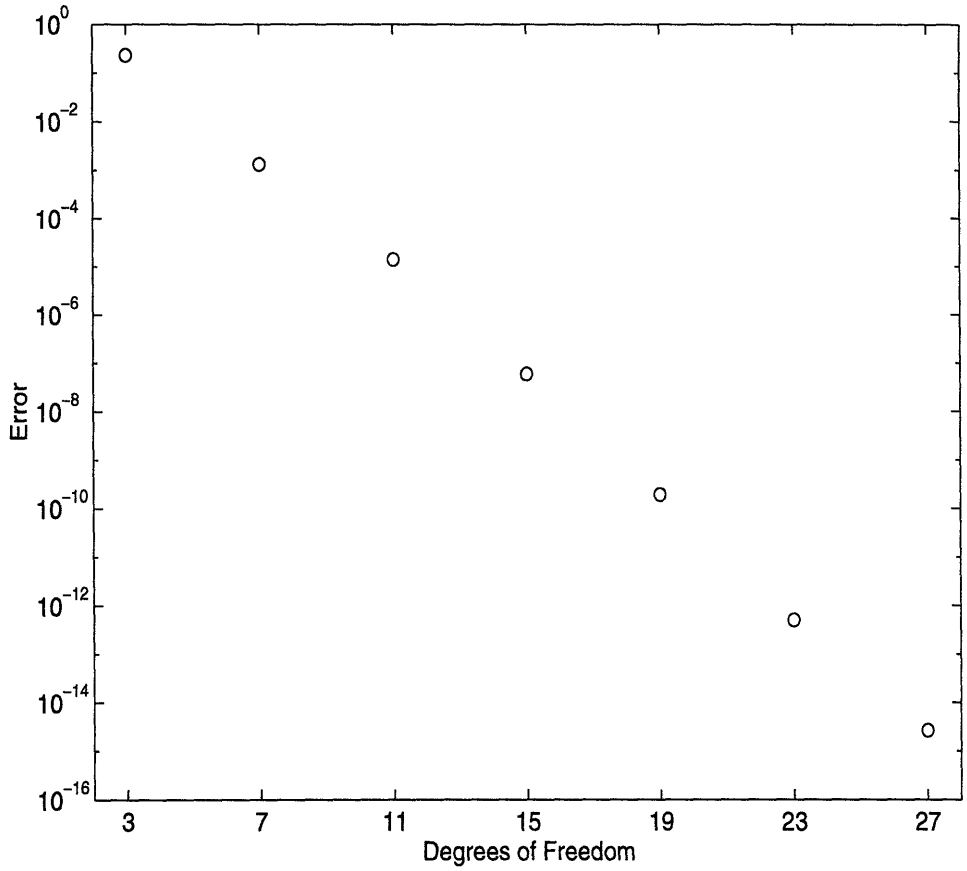

Figure B-1: Exponential convergence to an exact steady state solution of the forced Burgers' equation, $u_t - u_{xx} = f - uu_x$ with boundary conditions $u(0) = u(2\pi) = 0$ and forcing $f = (1 + \cos x) \sin x$. The maximum pointwise error for the steady state solution is plotted vs. degrees of freedom $(K * N - 1)$ with $K = 2$ elements.

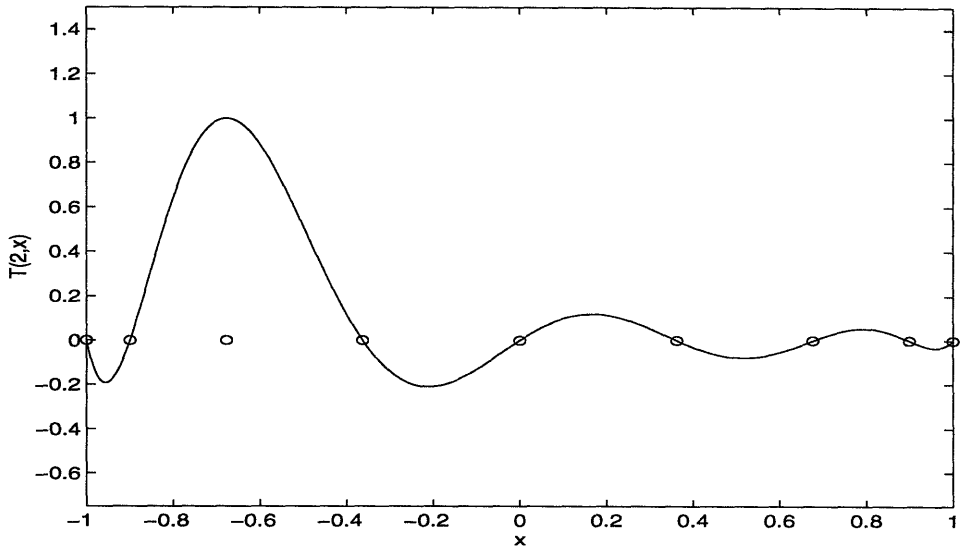

(a)

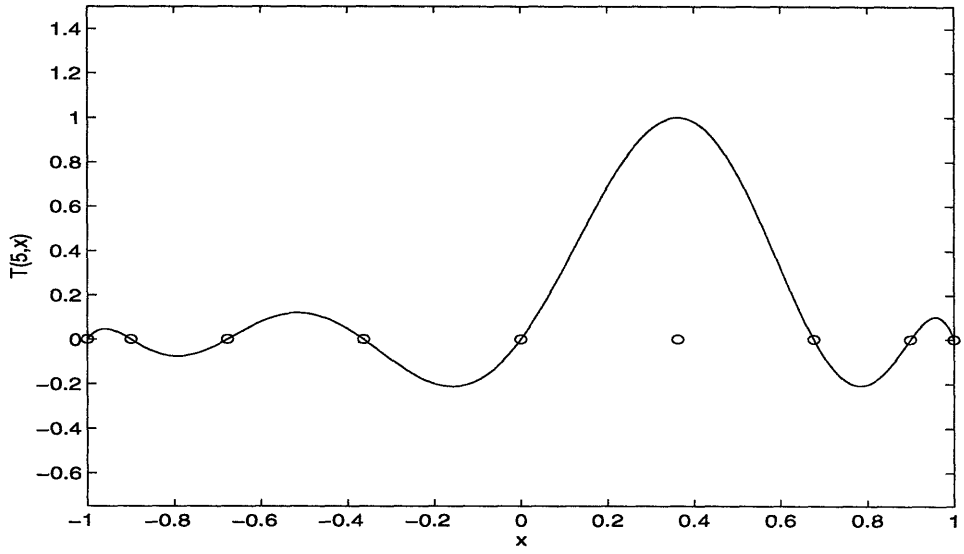

(b)

Figure B-2: Basis functions for Legendre-Lagrangian interpolation. o = Gauss-Lobatto collocation points for $N = 8$. In figure (a), $T_2(x)$ is plotted on $[-1, 1]$ and in figure (b), $T_5(x)$ is shown.

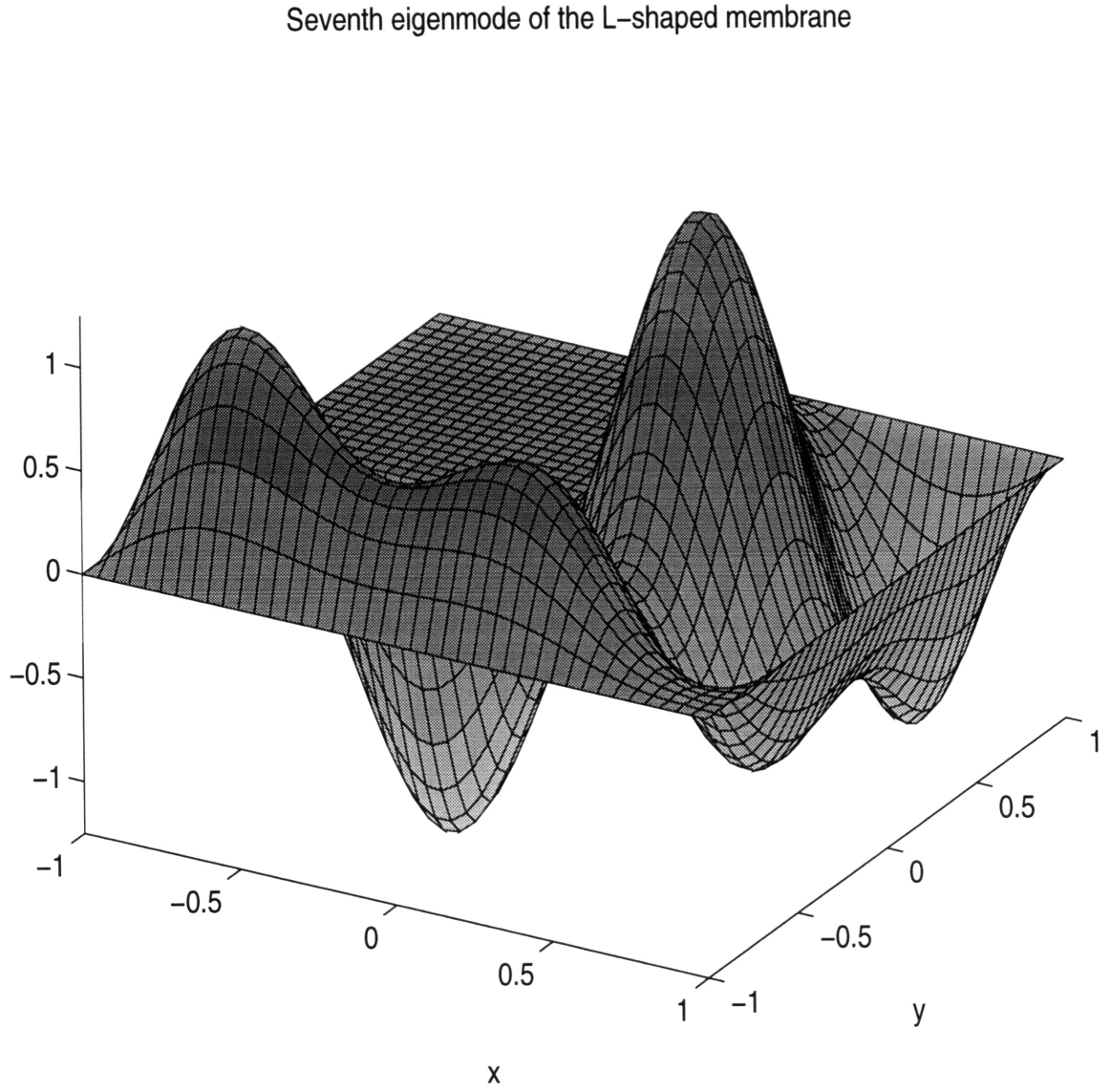

Figure B-3: Spectral element solution of $-\Delta u = \lambda u$ with $\lambda = 44.948$.

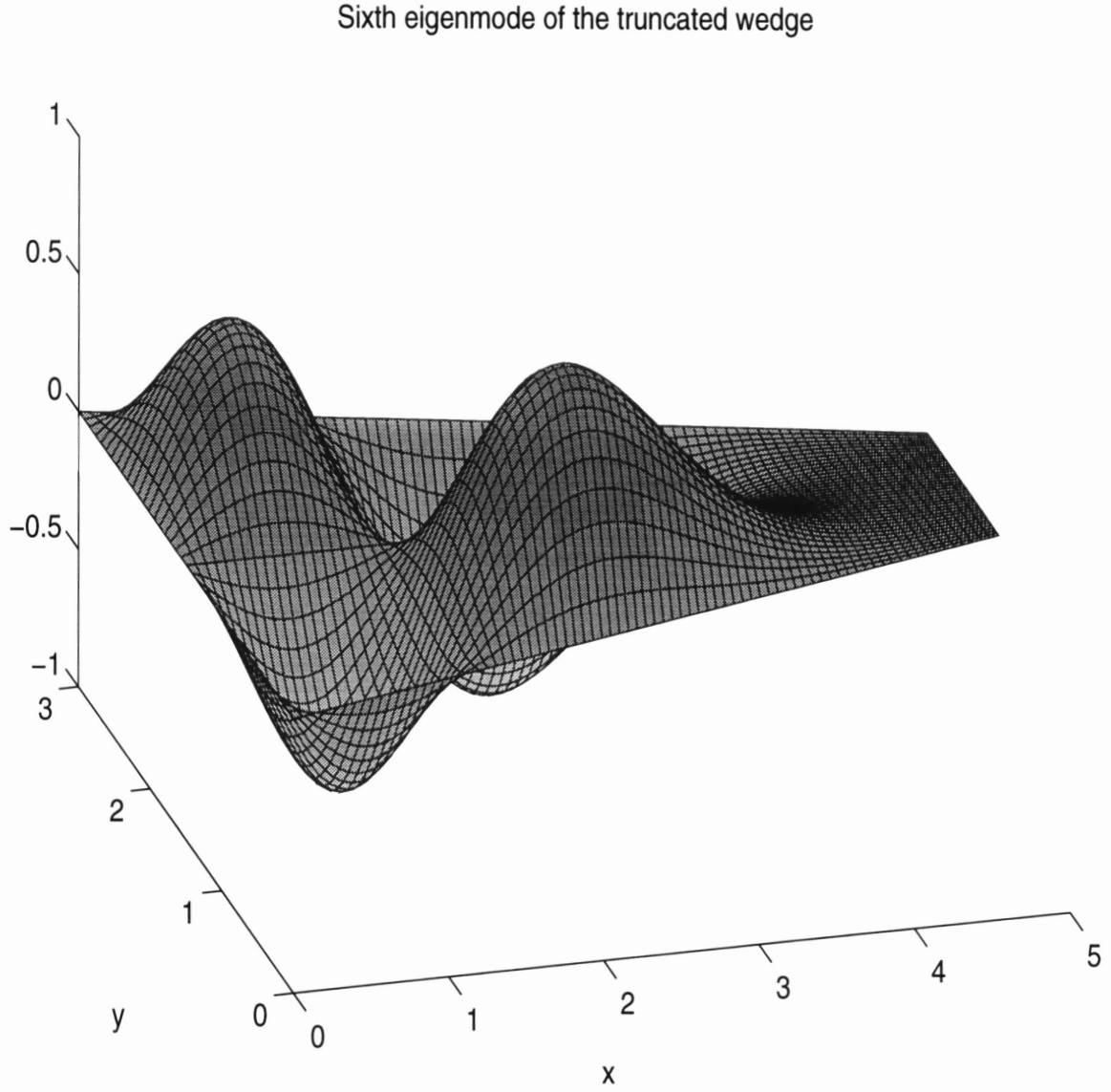

Figure B-4: Spectral element solution of $-\Delta u = \lambda u$ with $\lambda = 11.278$.

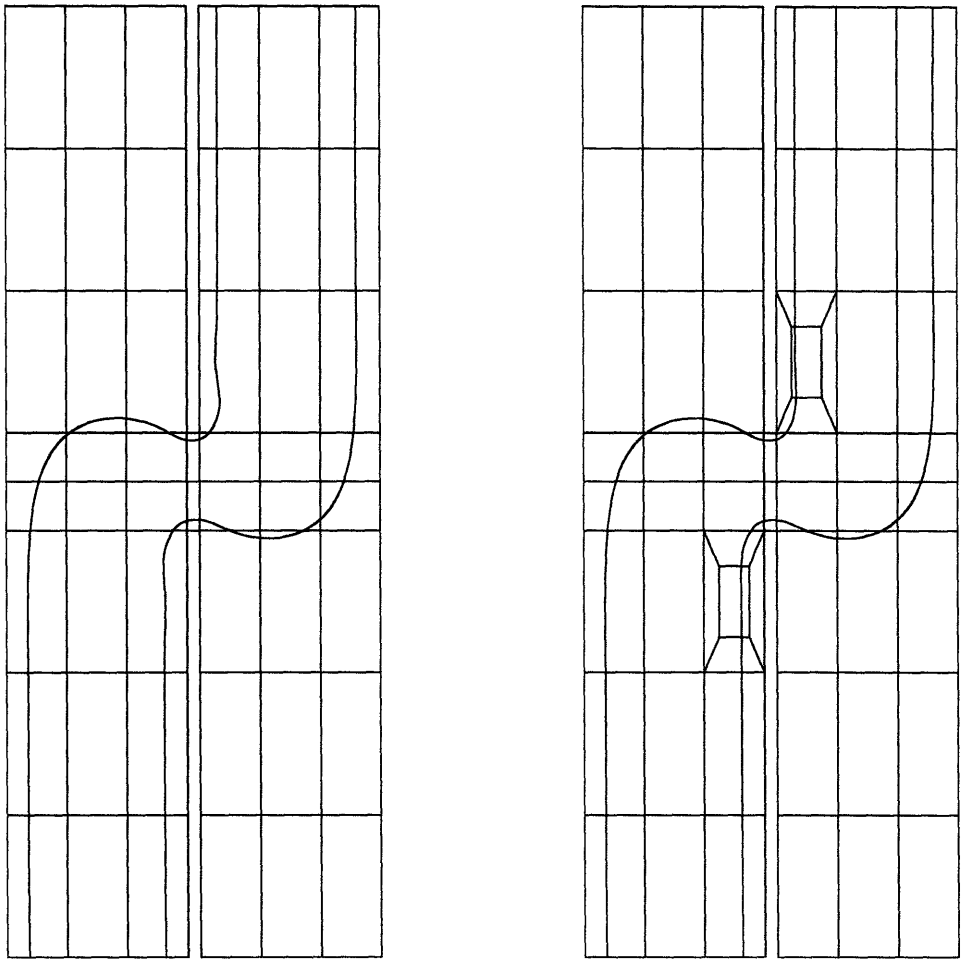

Figure B-5: Local refinement. Stokes flow through axial channels where all of the flux is diverted through the slot to the outer channel. In figure (a), $K = 50$ and $N = 4$. Near the slot, wiggles in the streamlines can be seen. Two elements are refined in figure (b) giving $K = 58$ and $N = 4$. Substantial improvement is obtained in the solution near the downstream edge of the slot.

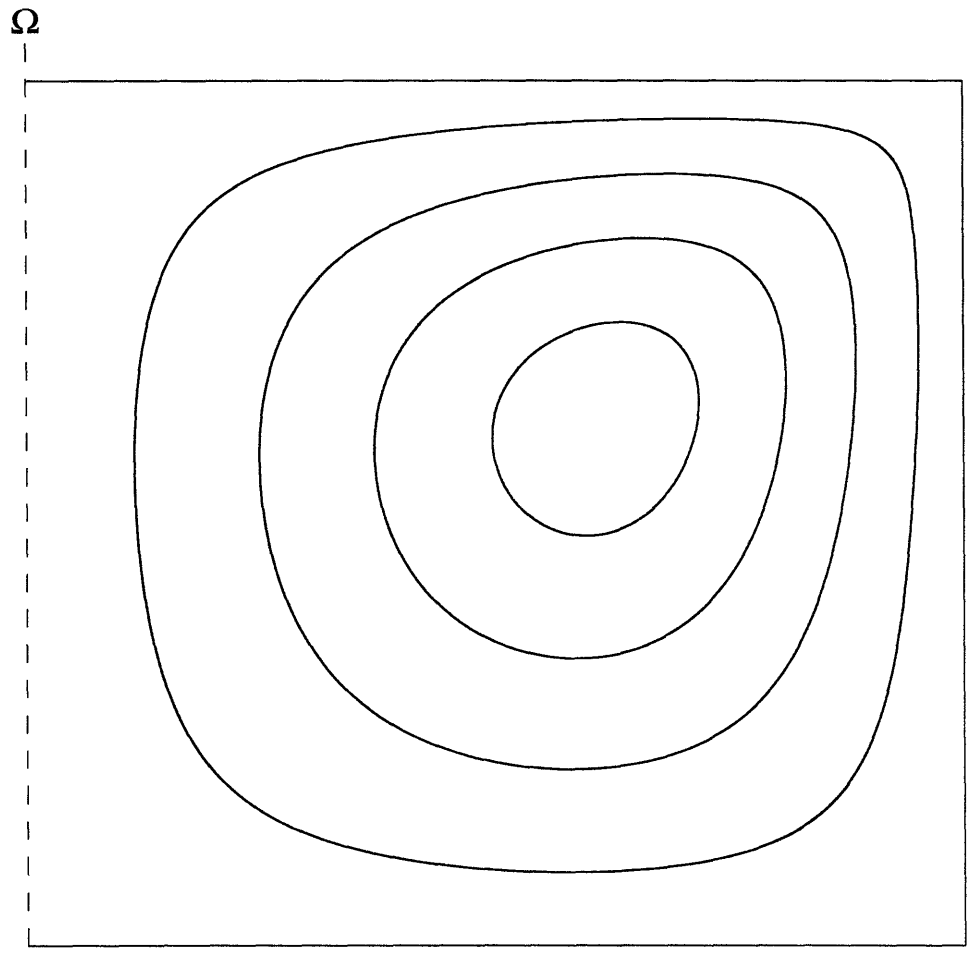

Figure B-6: Differential spin-up in a cylinder rotating at Ω. The top rotates at 1.3Ω. Clockwise rotation along steamlines.

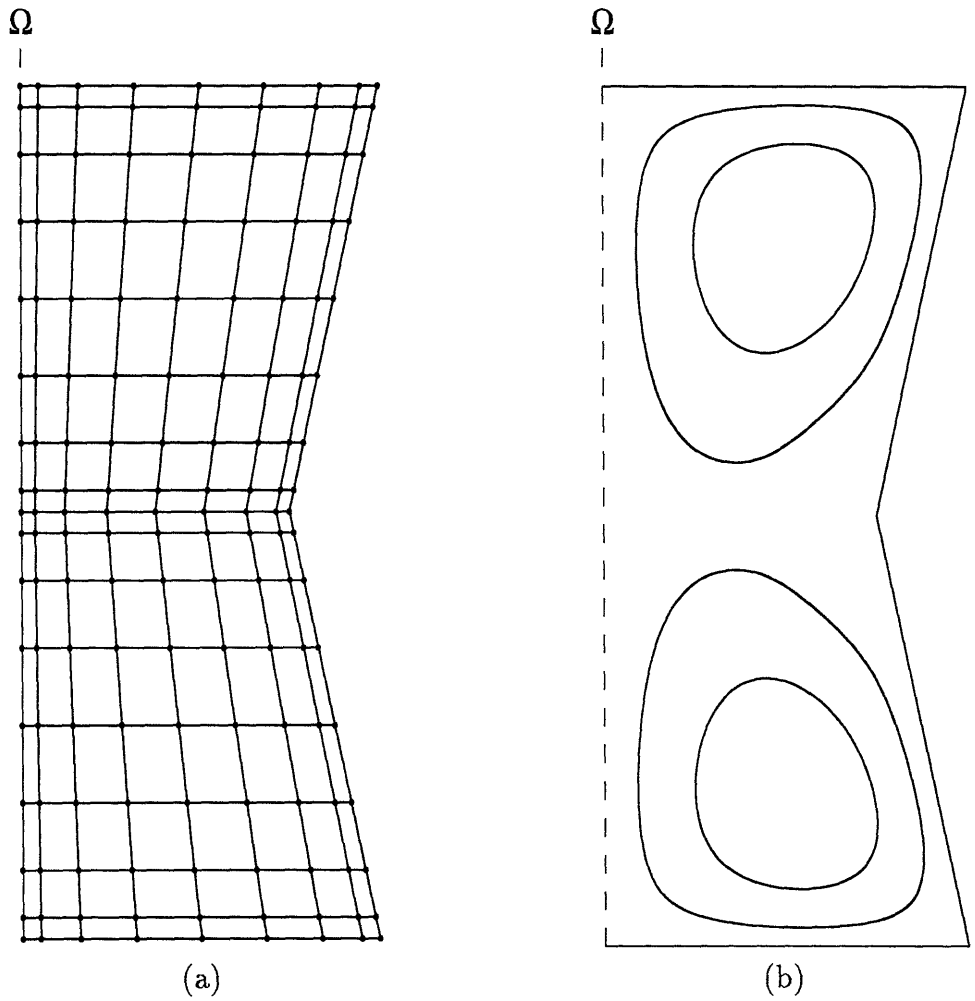

Figure B-7: Spin-up from rest in an hourglass shaped container. In figure (a) the two-element grid is shown along with the collocation points within each element. In figure (b) streamlines at time $t = 0.2$ are plotted. Their rotation is clockwise in the upper half of the container and counterclockwise in the lower half.

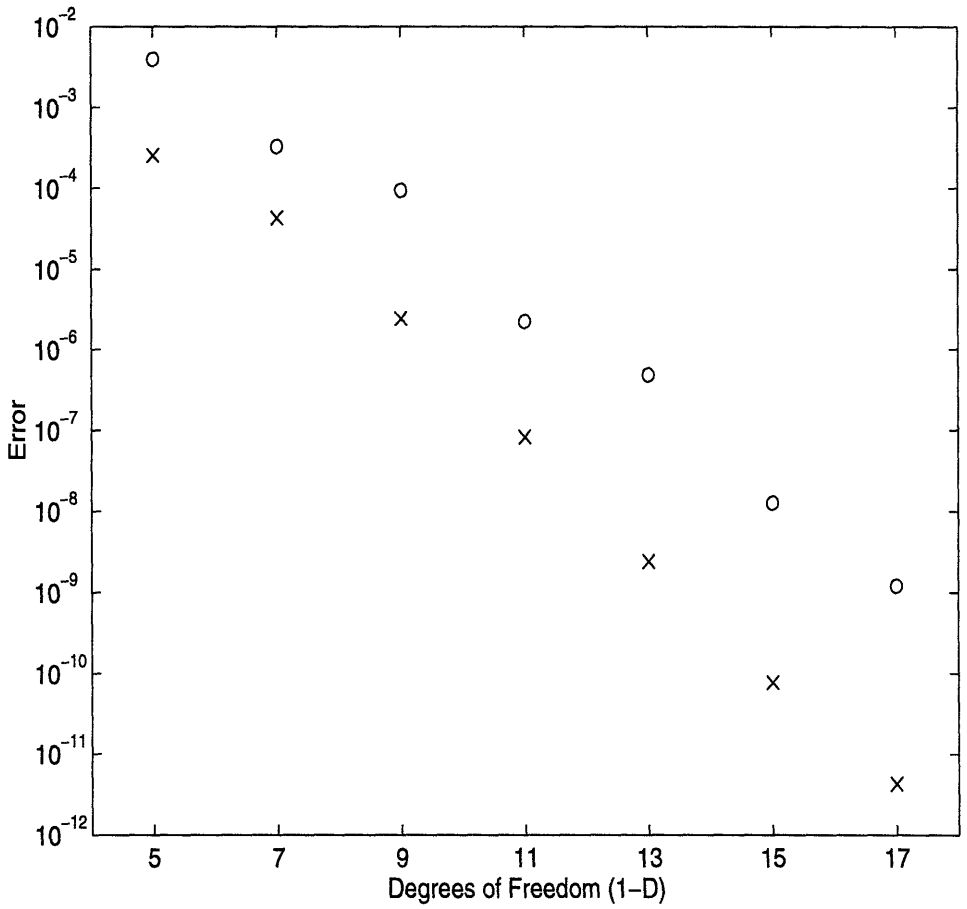

Figure B-8: Spectral accuracy of the incompressible, rotational Navier-Stokes equations is confirmed by exponential convergence to the exact steady state solution $p = \sin(\pi r)\sin(\pi z)$ and $u = v = r^3, w = -4r^2 z$. The cylindrical annulus $[1,2] \times [0,2\pi] \times [0,1]$ is broken into $K = 4$ elements in the $r - z$ plane. o = maximum pointwise error in the steady state pressure. $\times$ = maximum pointwise error in the steady state velocity.

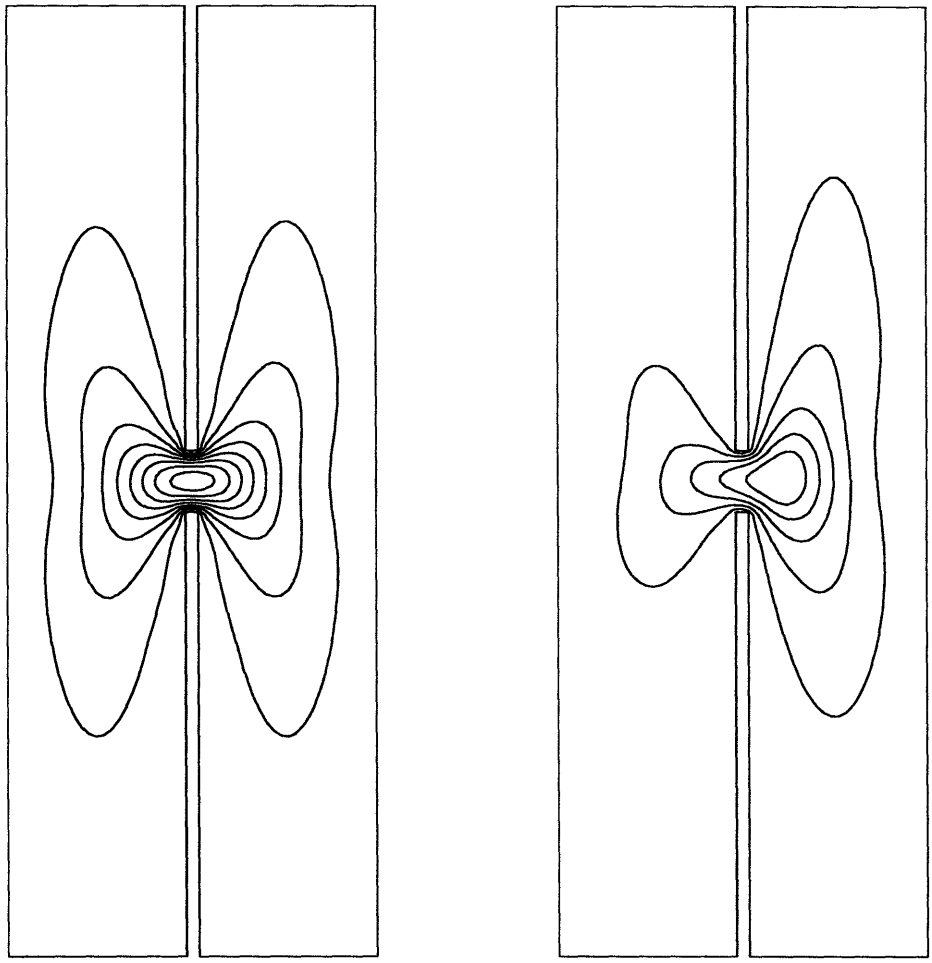

Figure B-9: The effects of nonlinearity on azimuthal motion. The Ekman number is $E = 1.6 \times 10^{-3}$ for both figures and contours of constant azimuthal velocity are shown. In figure (a) the Rossby number is $\mathcal{R}_0 = 8.0 \times 10^{-4}$ and the flow is fairly linear. In figure (b), $\mathcal{R}_0 = 8.0 \times 10^{-2}$. The swirl has been advected into the outer channel in perfect agreement with [1].

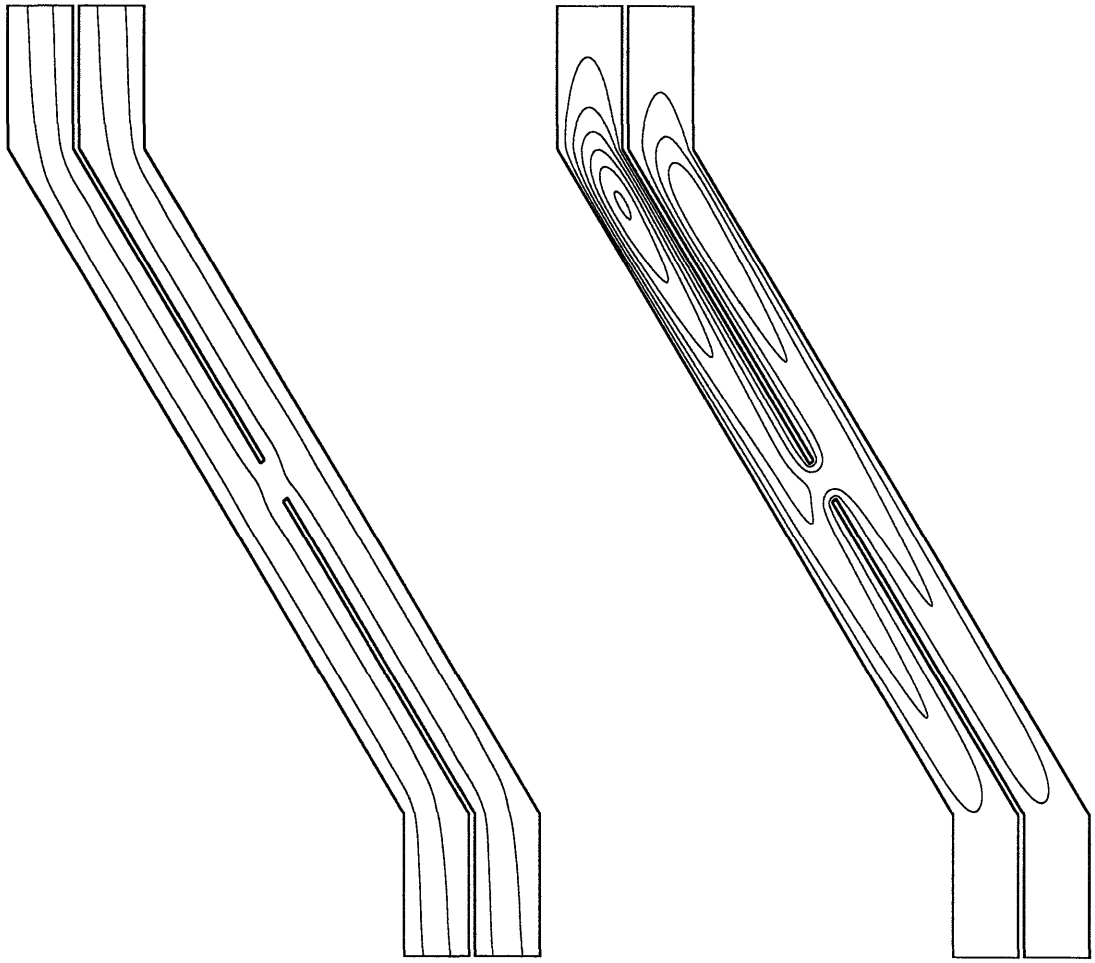

Figure B-10: Conical centrifuge. Wash channel design with $E = 1.6 \times 10^{-3}$ and $\mathcal{R}_0 = 8 \times 10^{-4}$. The geometry is broken up into $K = 86$ elements with $N = 4$ on each element. Streamlines are drawn in figure (a). In figure (b) contours of constant azimuthal velocity are plotted, $v = -3.0 + 0.5i, i = 0, \ldots, 5$.

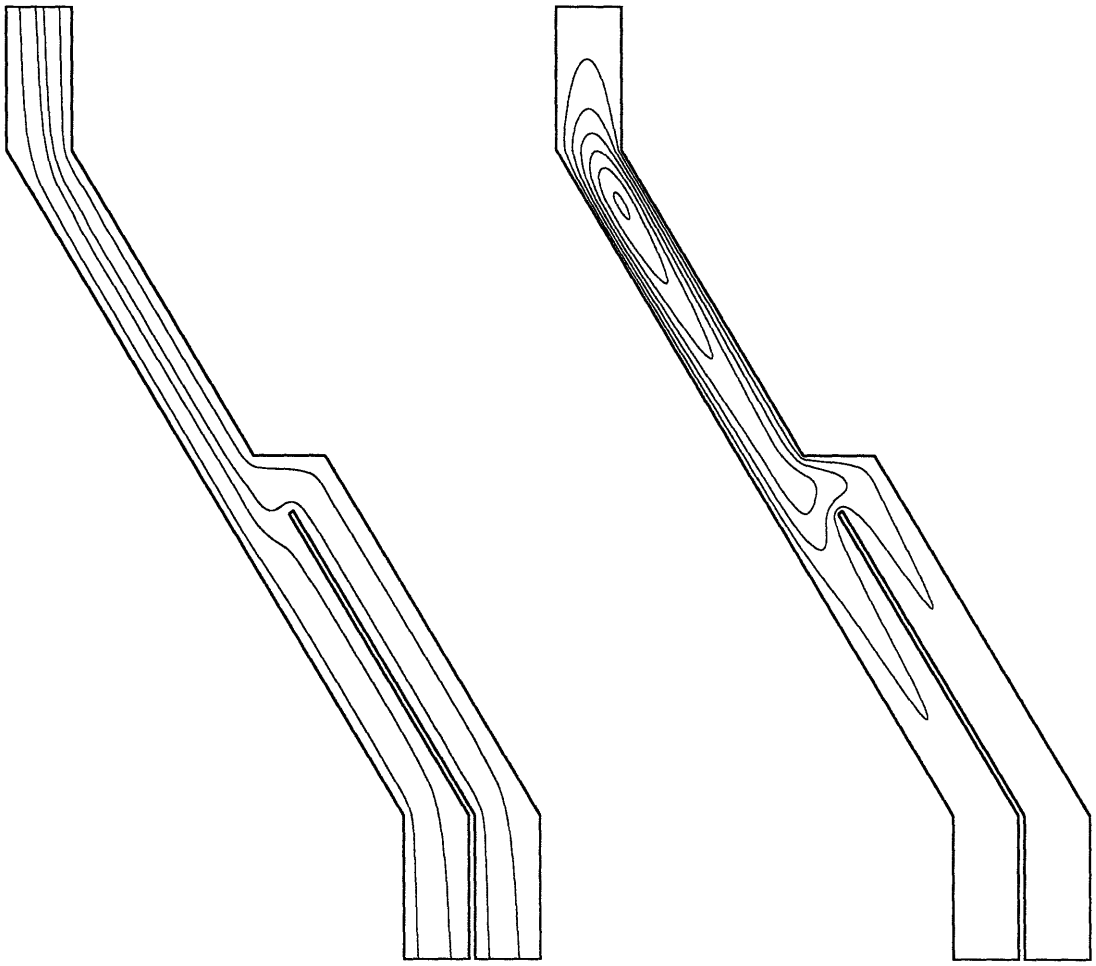

Figure B-11: Conical centrifuge. Half of the flux is diverted to the outer channel. In this case $E = 1.6 \times 10^{-3}$ and $\mathcal{R}_0 = 8 \times 10^{-4}$. The geometry is broken up into $K = 68$ elements with $N = 4$ on each element. Streamlines are drawn in figure (a). In figure (b) contours of constant azimuthal velocity are plotted, $v = -6.0 + 1.0i, i = 0, \ldots, 5$.

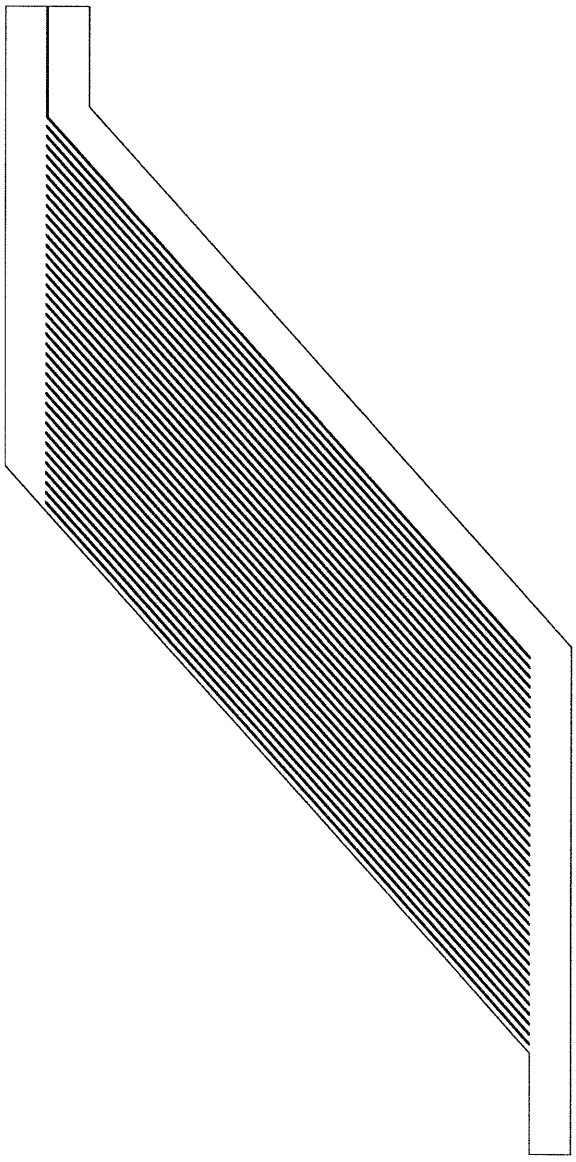

Figure B-12: Forty channel condensing centrifuge.

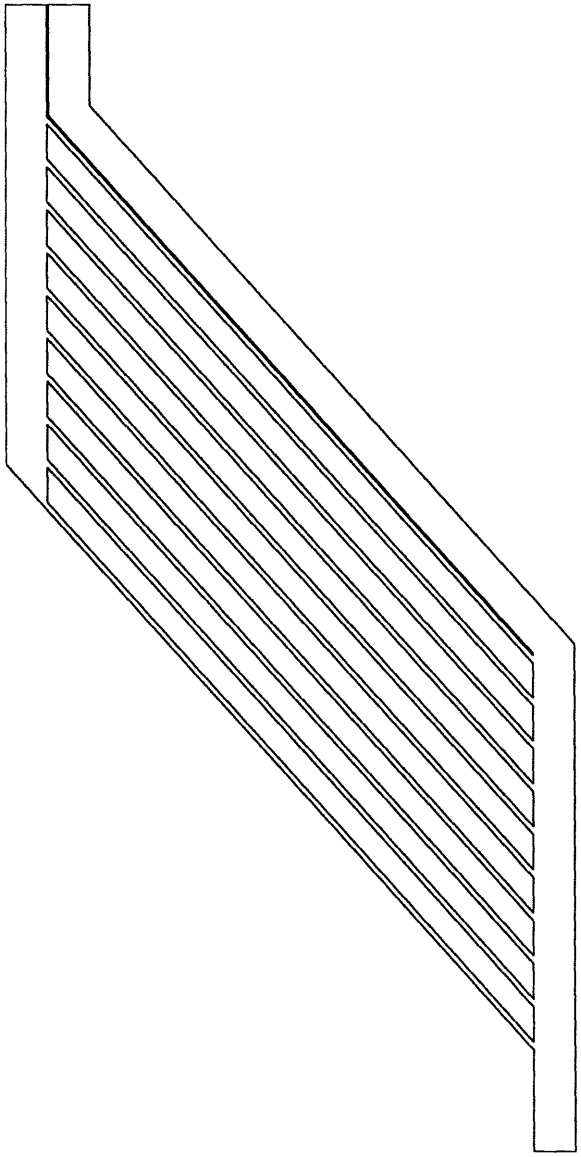

Figure B-13: Condensing centrifuge. Ten channel approximation.

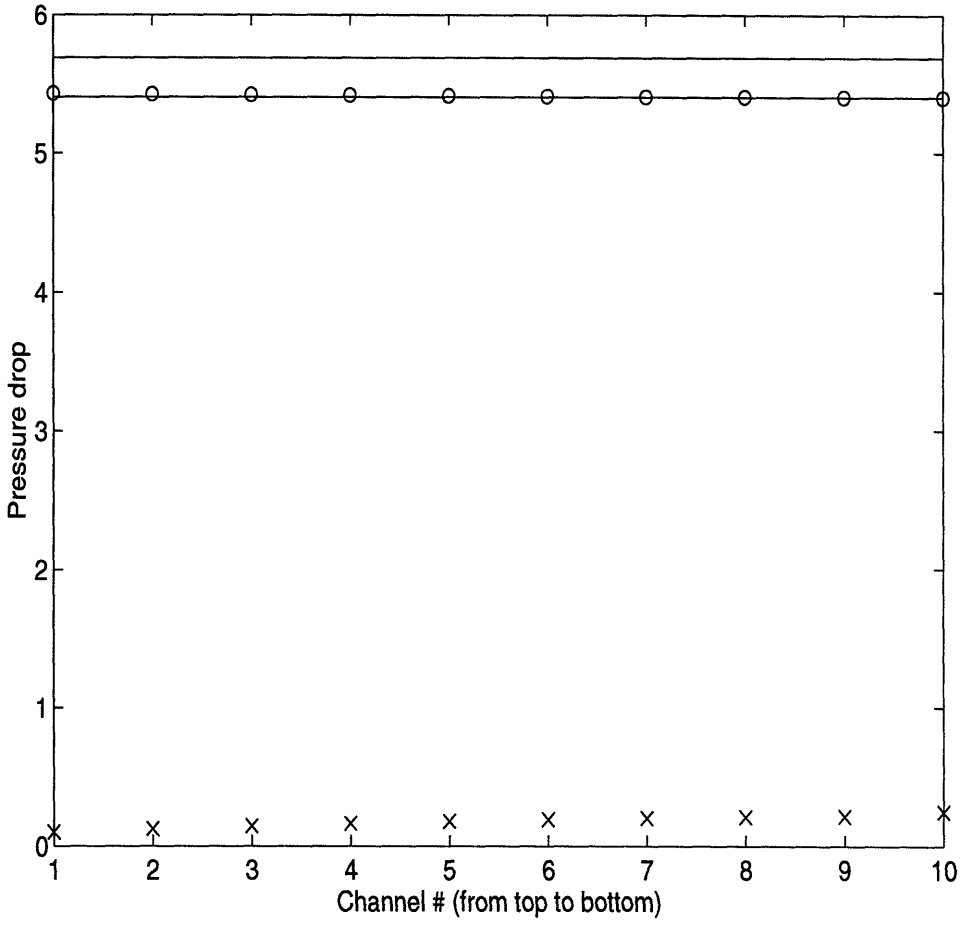

Figure B-14: Pressure drops in the ten channel condensing centrifuge. Top solid line: pressure difference between the top inlet and the top outlet. Bottom solid line: pressure difference between the bottom outlet and the top outlet. o = pressure difference between the channel inlet and the top outlet. × = pressure difference between the channel outlet and the top outlet.

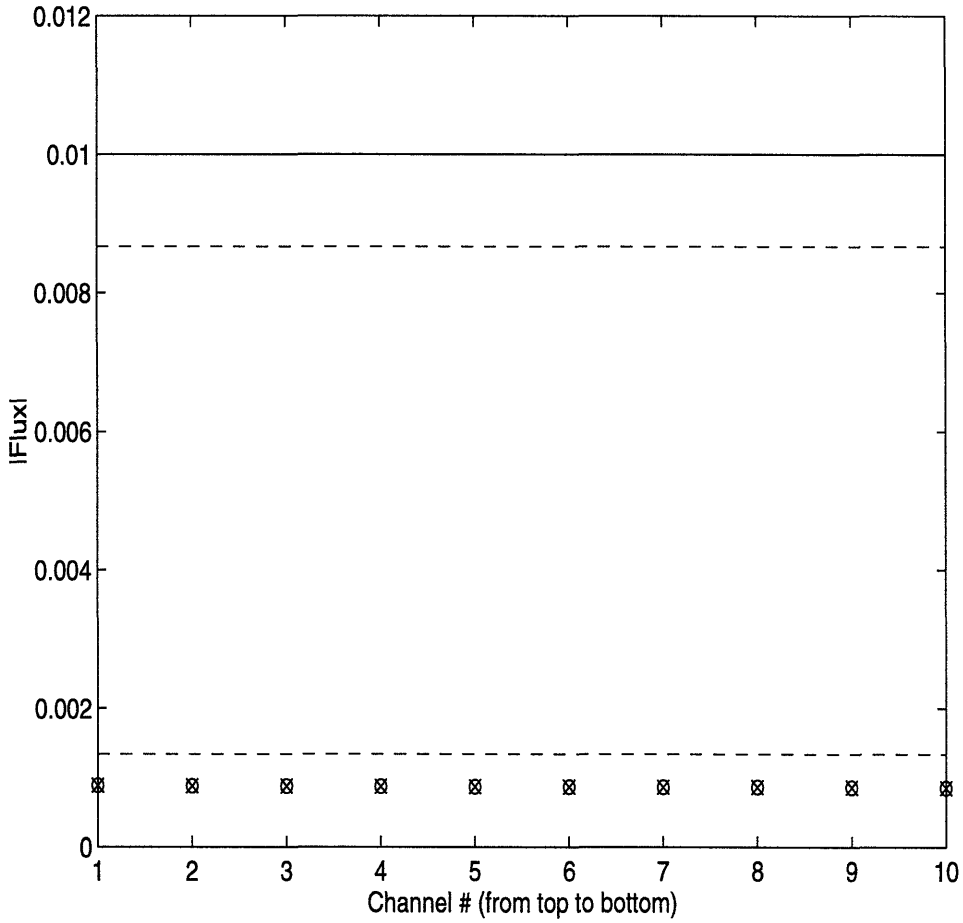

Figure B-15: Fluxes through the ten channel condensing centrifuge. Solid line: flux through the top inlet. Top dotted line: flux out of the top outlet. Bottom dotted line: flux out of the bottom outlet. o = flux through the channel inlet. $\times$ = flux through the channel outlet.